

## WHY DO ONLY SOME GALAXY CLUSTERS HAVE COOL CORES?

JACK O. BURNS<sup>1</sup>, ERIC J. HALLMAN<sup>1,2</sup>, BRENNAN GANTNER<sup>1</sup>, PATRICK M. MOTL<sup>3</sup>, MICHAEL L. NORMAN<sup>4</sup>  
*Draft version October 30, 2018*

### ABSTRACT

Flux-limited X-ray samples indicate that about half of rich galaxy clusters have cool cores. Why do only some clusters have cool cores while others do not? In this paper, cosmological N-body + Eulerian hydrodynamic simulations, including radiative cooling and heating, are used to address this question as we examine the formation and evolution of cool core (CC) and non-cool core (NCC) clusters. These adaptive mesh refinement simulations produce both CC and NCC clusters in the same volume. They have a peak resolution of  $15.6 h^{-1}$  kpc within a  $(256 h^{-1} Mpc)^3$  box. Our simulations suggest that there are important evolutionary differences between CC clusters and their NCC counterparts. Many of the numerical CC clusters accreted mass more slowly over time and grew enhanced cool cores via hierarchical mergers; when late major mergers occurred, the CC's survived the collisions. By contrast, NCC clusters experienced major mergers early in their evolution that destroyed embryonic cool cores and produced conditions that prevented CC re-formation. As a result, our simulations predict observationally testable distinctions in the properties of CC and NCC beyond the core regions in clusters. In particular, we find differences between CC versus NCC clusters in the shapes of X-ray surface brightness profiles, between the temperatures and hardness ratios beyond the cores, between the distribution of masses, and between their supercluster environs. It also appears that CC clusters are no closer to hydrostatic equilibrium than NCC clusters, an issue important for precision cosmology measurements.

*Subject headings:* cool cores — galaxies: clusters: general — cosmology: theory — hydrodynamics — methods: numerical — intergalactic medium

### 1. INTRODUCTION

Clusters of galaxies with “cool cores” have peaked X-ray emission (*i.e.*, excess above that extrapolated inward from a  $\beta$ -model fit of the X-ray profile beyond the core) coincident with supergiant elliptical galaxies. They have central cooling times typically  $< 0.1 H_o^{-1}$  and central gas temperatures  $\approx 30$ -40% of the virial temperatures (*e.g.*, Ikebe et al. 1997; Lewis et al. 2002; Peterson et al. 2003). Cores of cool gas are found to be common in flux-limited samples, although a selection bias is likely present because of the strongly peaked X-ray emission in these clusters. From a sample composed of clusters detected with *Einstein*, White et al. (1997) found cool cores (CC) in  $\approx 60\%$  of their 207 cluster sample. From a sample of 55 flux-limited *ROSAT*-observed clusters, Peres et al. (1998) found CCs in over 70% of their galaxy clusters. More recently, Chen et al. (2007) identified 49% of their 106 clusters as having cool cores in a flux-limited sample, HIFLUGCS, based upon both *ROSAT* and *ASCA* observations.

Why do some, but not all, galaxy clusters contain cool cores? To answer this question, we must explore the origin and evolution of cool cores galaxy clusters. The earliest and simplest model assumed clusters to be spherical,

isolated systems where “cooling flows” formed; as radiating gas loses pressure support, cooling gas flows inwards to higher density values which further accelerates the cooling rate (*e.g.*, Fabian 2002). But, the predicted end-products of this mass infall (*e.g.*, star formation, HI, CO) have not been observed and the central temperatures indicate that the gas at the cores has only moderately cooled (see review by Donahue & Voit 2004). The current paradigm calls for heating to offset cooling, possibly by AGNs via strong shocks (*e.g.*, Heinz et al. 1998) or weak shocks (*e.g.*, Fabian et al. 2003), or by AGNs + thermal conduction (*e.g.*, Ruszkowski et al. 2004), or by AGNs + preheating (*e.g.*, McCarthy et al. 2007a), or by Alfvén waves induced by AGNs in the inner core and cluster mergers in the outer cores (*e.g.*, Fujita et al. 2007).

The simple cooling flow model did not incorporate the important effects of mergers and on-going mass accretion from the supercluster environment in which these clusters reside (*e.g.*, Motl et al. 2004; Poole et al. 2006). Burns et al. (1997) and Gómez et al. (2002) first examined the result of cluster collisions in 2-D numerical simulations that involved two idealized spherical clusters with  $\beta$ -model density profiles and central cool cores that collided together head-on. They found that the ram pressure from major mergers (*i.e.*, subcluster to cluster mass ratios of  $\approx 15\%$  to 100%) tends to disrupt the cool cores. Similarly, Ritchie & Thomas (2002) and Ricker & Sarazin (2001) found disruptions of cool cores by major mergers between spherical clusters using 3-D simulations. These numerical models may suggest that the numbers of cool cores diminish as clusters grow via mergers (*i.e.*, fewer cool cores in richer clusters at smaller  $z$ ).

Electronic address: jack.burns@cu.edu

<sup>1</sup> Center for Astrophysics and Space Astronomy, Department of Astrophysical & Planetary Science, University of Colorado, Boulder, CO 80309

<sup>2</sup> National Science Foundation Astronomy and Astrophysics Postdoctoral Fellow

<sup>3</sup> Department of Physics and Astronomy, Louisiana State University, Baton Rouge, LA 70803

<sup>4</sup> Center for Astrophysics and Space Sciences, University of California-San Diego, 9500 Gilman Drive, La Jolla, CA 92093

More recently, we performed numerical simulations of the formation and evolution of clusters in a cosmological context using the adaptive mesh refinement N-body/hydro code *Enzo*, aimed at further understanding cool cores (Burns et al. 2004; Motl et al. 2004). The gas in these clusters was evolved with radiative cooling but no heating. We found that cooling modifies not only the cores but also significantly alters the cluster appearance out to the virial radius (see also Akahori & Masai 2006). As new subcluster halos fall into a cluster, they gradually donate cool gas so that the cool cores grow over time. Most mergers are oblique with halos spiraling into the cluster centers and gently bequeathing cool gas to enhance the cores. Thus, in this model, cool cores themselves grow hierarchically via the merger/accretion process. This model predicts that even cool core clusters should possess a variety of substructures such as bullet subclusters and cold fronts, similar to those observed in Abell clusters (*e.g.*, Hallman & Markevitch 2004; Markevitch et al. 2002; Markevitch & Vikhlinin 2007). It also suggests cool cores may grow stronger (*i.e.*, cooler and denser) as rich clusters increase in mass at recent epochs.

The Motl et al. (2004) simulations were limited by the baryonic physics that included only radiative cooling. This model suffers from the well-known cooling catastrophe (*e.g.*, White & Rees 1978) that results in an overproduction of cool cores and an increase in the baryon fraction (*e.g.*, Kravtsov et al. 2005). Nearly every dark matter potential well in this simulation was occupied by a halo of gas that had cooled significantly. Furthermore, these cool cores are “hard”, generally denser, colder, and with more distinct boundaries than are observed. The steep density contrast shelters the cores from ram pressure stripping, thus allowing them to survive and grow robustly during mergers with other halos. Clearly, a more realistic model of cool cores must involve added physical processes that “soften” the cores, thus making some susceptible to disruption during mergers. Heating by star formation (*e.g.*, Valdarnini 2006b) or by AGNs would potentially soften the cores. Additional softening effects may include thermal conduction (*e.g.*, Zakamska & Narayan 2003; Ruszkowski & Begelman 2002) along with mixing/heating from radio jet/lobe entrainment, and weak shocks and turbulent heating arising from halo mergers (*e.g.*, Burns 1998; Brügggen & Kaiser 2002; Fujita et al. 2004; Voit & Donahue 2005; Mathews et al. 2006).

In this paper, we present *Enzo* cosmology simulations that include radiative cooling, star formation (*i.e.*, a mass sink for cold gas), and heating (see also Motl et al. 2005; Hallman et al. 2006). Unlike previous simulations, our cooling + heating prescription has succeeded in producing both cool core and non-cool core clusters within the same computational volume. In addition to the somewhat more realistic baryonic physics, these simulations have the advantage of bigger volumes and larger samples of clusters than in previous computational simulations (Motl et al. 2004; Kravtsov et al. 2005). Thus, we have the dataset to examine evolutionary effects in these numerical clusters and can address the question in the title of this paper with good statistics. In Section 2, we describe the new simulations and the analysis of the numerical clusters. In Section 3, we compare the statistical

properties of our numerical clusters with recent observed samples and show that the agreement is good. In Section 4, we describe new insights into the formation of cool core (CC) and non-cool core (NCC) clusters from our simulations. In Section 5, we describe the observational consequences of evolutionary differences in CC and NCC clusters. Conclusions and a summary are presented in Section 6.

## 2. NUMERICAL SIMULATIONS

The simulations described in this paper were performed with the *Enzo*<sup>5</sup> code (O’Shea et al. 2004) that couples an N-body algorithm for evolving the collisionless dark matter particles with an Eulerian hydrodynamics scheme (PPM) that utilizes adaptive mesh refinement. We adopt a  $\Lambda$ CDM cosmology with  $\Omega_b = 0.026$ ,  $\Omega_m = 0.3$ ,  $\Omega_\Lambda = 0.7$ ,  $h = 0.7$ ,  $n_s=1$ , and  $\sigma_8 = 0.9$ . The simulation was initialized at  $z=30$  using the CDM transfer function from Eisenstein & Hu (1999). A low-resolution simulation was first used to identify clusters in a volume of  $256 h^{-1}$  Mpc on a side using  $128^3$  dark matter particles and grid zones. High-resolution simulations were then performed that evolved the entire volume but adaptively refined 50 smaller regions (as separate simulations) around the largest clusters identified on the low resolution grid. Each of these 50 regions first is refined with two levels of static nested grids, each having a cell size half that of its parent grid (thus each region has spatial resolution 4 times better than the parent grid). Within the nested grids, the dark matter particles have a mass resolution of  $9 \times 10^9 h^{-1} M_\odot$ . Then, within the nested static grids, we evolve the simulation with 5 additional levels of adaptive refinement, again with a factor of two increase in spatial resolution at each level. Cells are flagged for refinement based on the local baryonic and dark matter overdensities, refining on thresholds of 8.0 times the minimum value at that level. The spatial resolution on the finest grid is  $15.6 h^{-1}$  kpc, adequate to resolve the cool core ( $r_{CC} \approx 100 h^{-1}$  kpc), but not to probe the details of its structure (see also Motl et al. 2004).

Radiative cooling is calculated from a tabulated cooling curve derived from a Raymond-Smith plasma emission model (Brickhouse et al. 1995) assuming a constant metallicity of 0.3 relative to solar. The cooling curve is truncated below a temperature of  $10^4$  K. Every timestep, we calculate the energy radiated from each cell and remove that amount of energy from the cluster gas (Motl et al. 2004).

As mentioned above, star formation provides one mechanism to soften cool cores by both transforming rapidly cooling gas into star particles (and, therefore, removing the cold gas) and by heating the surrounding gas with energy injected from supernovae. The star formation and heating that we used follows the prescription outlined by Cen & Ostriker (1992) and described in Burns et al. (2004). In brief, the code examines all grid cells at the finest refinement level above a specified overdensity. The gas is converted to collisionless “star” particles when it is undergoing compression, rapid cooling, and the mass in the cell exceeds the Jean’s mass. The star formation rate is coupled to the local dynamical time and to a user-specified star formation

<sup>5</sup> <http://lca.ucsd.edu/portal/software/enzo>

efficiency. Once formed, the new star particle deposits energy in the gas to simulate the instantaneous feedback from Type II supernovae. The strength of the supernova feedback is controlled by another efficiency parameter,  $\epsilon$ , which gives the thermal energy injected in proportion to the estimated rate of star formation for that particle ( $\dot{M}_{star} = M_{star}/t_{dyn}$ , and  $\dot{e} = \epsilon \dot{M}_{star} c^2$ ). The most important parameter in the star formation recipe was found to be the strength of thermal feedback from prompt supernovae. Through trial and error, we found that the value of  $\epsilon = 4.11 \times 10^{-6}$  yields a reasonable fraction of baryons locked in star particles at the current epoch (see also Burns et al. 2004). This value for the feedback parameter corresponds to (for a star formation rate of one solar mass per year) a supernovae rate of one per century with an average energy generation of  $7 \times 10^{50}$  ergs per supernova. The chosen star formation parameters also produce both CC and NCC clusters in the same volume.

In Figure 1, we show a representative example of a cool core cluster at  $z = 0$  including images of the bolometric X-ray surface brightness, emission-weighted temperature, and the distribution of star particles (see Hallman et al. (2006) for details on construction of synthetic X-ray and temperature images). These images illustrate the dynamic range in X-ray structures and temperatures typical in simulations of CC clusters, including the off-center infall of lower mass cool halos with leading bow shocks. The star particle image shows the distribution of sinks of cold gas and extended heating as new halos are accreted.

The average total energy injection rate for the 10 most massive CC and 10 NCC clusters with a comparable mass distribution (at  $z = 0$ ) within our computational volume is  $\approx 5 \times 10^{43}$  ergs/sec. This is comparable to the X-ray luminosity for these clusters, thus our prescription produces an approximate balance between heating and cooling. This energy injection rate is also similar to the typical kinetic luminosities thought to power radio jets/lobes in central cluster radio sources (*e.g.*, Burns 1990; Eilek & Owen 2006; Gentile et al. 2007; Wise et al. 2007). Thus, we view this energy injection scheme as a generalization of pre-heating of the core from a variety of sources, including AGN. The average energy injection rate is approximately the same over all epochs between  $z \approx 1$  and  $z = 0$ . This feedback is also comparable for CC and NCC clusters of the same mass suggesting, as we show in Section 4, that something other than feedback, namely mergers, drive the evolution of these two cluster types.

We constructed a catalog of all numerical clusters with  $M_{200} > 10^{14} M_{\odot}$  from  $z=0$  to  $z=2$ . ( $M_{200}$  is measured out to the radius,  $r_{200}$ , where the density is 200 times the critical density and is  $\approx M_{virial}$  which we will use interchangeably throughout this paper.) At  $z = 0$ , we have 94 clusters in the sample, but the entire catalog out to  $z = 2$  contains 1522 clusters (many are the same cluster but at different epochs) giving us one of the largest samples of numerical rich clusters to date from a cosmological simulation. These cluster simulations are publicly archived<sup>6</sup>. We have constructed a master table of the basic properties of these clusters including the average

emission-weighted temperatures, virial and gas masses,  $r_{200}$  ( $\approx$  the virial radius), baryon fractions,  $\beta$ -model fit parameters, CC or NCC designation, and other properties. The archive and this table will be presented in Hallman et al. (2007). These archived clusters form the basis of the analysis of numerical clusters presented in this paper.

After visually inspecting all the temperature profiles for the  $z = 0$  clusters, we defined a cool core cluster to be one that has a  $\geq 20\%$  reduction in the central temperature compared to the surrounding region (where the slope of the temperature profile becomes negative; see Figure 7) and this candidate baryonic cool core is within one zone ( $\approx 16 h^{-1}$  kpc) of the dark matter density peak. This is a conservative definition that will yield the smallest number of cool cores, but we estimate that more liberal definitions will not increase the number by more than  $\approx 10\%$ . With this strict classification, we find that 16% of all the numerical clusters with  $M_{200} > 10^{14} M_{\odot}$  have cool cores. This is low relative to the most recently observed fraction of 49% (Chen et al. 2007) that comes from a flux-limited sample (which may be biased somewhat high by flux boosting from the cool cores). Several possible effects may be operating to reduce the fraction of numerical CC clusters. First, our baryon fraction (2.6%) for this simulation is now recognized as low relative to the recent value from WMAP III (4.2%, Spergel et al. (2007)). A higher gas fraction could result in more robust cool cores. Second, the power spectrum normalization ( $\sigma_8$ ) may play a role in determining the number of CC clusters (our current value of  $\sigma_8$  is larger than that inferred from WMAP III). Third, the numbers of cool cores and their survival during mergers appear to be a sensitive function of the heating/cooling prescription. Fourth, numerical resolution is likely a factor in the production of cool cores.

### 3. STATISTICS OF THE X-RAY PROPERTIES OF CC AND NCC NUMERICAL CLUSTERS

How well do the general characteristics of our numerical clusters match real galaxy clusters? This is an important question to address before we propose a new formation scenario for cool core and non-cool core clusters based upon our numerical simulations.

In the analysis that follows, we calculated the projected average temperatures for our simulated clusters as “spectroscopic-like” temperatures as in Rasia et al. (2005). The weighting of temperature is different from the standard emission-weighted temperature, and has been shown to be more consistent with the value of the temperature which would be deduced from an X-ray spectral fit. The calculation performs

$$T_{500SL} = \frac{\int n^2 T^a / T^{1/2} dV}{\int n^2 T^a / T^{3/2} dV}, \quad (1)$$

where  $a=0.75$  is the value fitted from Mazzotta et al. (2004) which best approximates the value of the spectroscopic temperature from X-ray fitting. In our case we have integrated this weighting in a cylinder with a radius of  $r_{500}$  around the cluster center.

In Figure 2, the distributions of  $M_{200}$  and  $T_{500SL}$  (spectroscopic-like temperature inside  $r_{500}$ ) for the overall catalog of clusters, as well as for CC and NCC clusters

<sup>6</sup> <http://lca.ucsd.edu/data/sca>

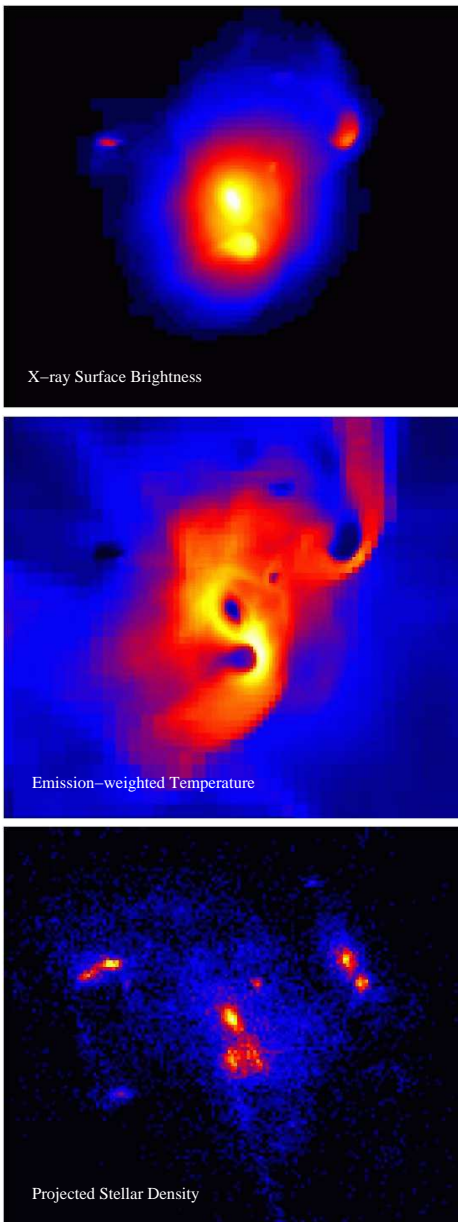


FIG. 1.— Representative example of a cool core cluster with  $M_{200} = 5 \times 10^{14} M_{\odot}$  and  $T_{\text{virial}} = 4.2$  keV at  $z = 0$  from the AMR simulation volume. The top image is projected synthetic X-ray surface brightness. The middle image is emission-weighted temperature (blue is  $T < 4$  keV and yellow is  $T > 5$  keV). The bottom image is a projection of the star particle density. The field of view is  $3.5 h^{-1}$  Mpc. Within the catalog, are shown. We eliminated the cool core regions in calculating  $T_{500SL}$  so as not to bias these temperature measurements and to use a technique similar to that applied to observations. As will be discussed further in Section 5, there are fewer high mass, high temperature CC clusters in comparison to NCC clusters in the catalog. At  $z = 0$ , the average mass of the CC clusters is  $2.4 \pm 1.4 \times 10^{14} M_{\odot}$  and that of the NCC clusters is  $4.7 \pm 3.4 \times 10^{14} M_{\odot}$ .

In Figure 3, we show examples of the most reliable statistics and basic relationships between variables that are typically calculated from X-ray observations. We compare these numerical data for  $z < 1$  clusters (to approximately match the range of redshifts for current observations) in our catalog with those obtained from the

recent statistically complete sample of clusters observed with *ROSAT* and *ASCA* as reported by Chen et al. (2007). The numerical clusters were separated into CC and NCC using the criteria noted in Section 2. In the top panel of Figure 3, we plot the core radius versus the slope ( $\beta$ ) for a  $\beta$ -model fit to the synthetic X-ray surface brightness profile ( $S_X \propto [1 + (r/r_c)^2]^{1/2-3\beta}$ ). For the CC clusters, the cool cores were excluded from the fit (see Section 5.2 for details). This plot shows a separation between CC and NCC clusters such that cool core clusters have smaller cores,  $r_c$ , for a given  $\beta$ . This separation and the overall results from these  $\beta$ -model fits match up very well with Figure 3 in Chen et al. (2007).

The second panel shows the mean gas fraction measured out to  $r_{500}$  ( $f_{gas}(r_{500}) = \langle \rho_{gas}/\rho_{total} \rangle_{500}$ ) as a function of  $T_{500SL}$ . We attempted to correct our gas fractions by multiplying  $f_{gas}$  by the ratio of  $\Omega_b$  measured by WMAP III to that which we used in these simulations (Section 2). This brings our gas fractions into somewhat better agreement but we emphasize that they are still low relative to recent observations (e.g., McCarthy et al. 2007b; Vikhlinin et al. 2006b; Sadat et al. 2005). We do find good qualitative agreement in the shape and distribution of points in this figure relative to Figure 13 in Chen et al. (2007). There may be a slight tendency for reduced gas fractions at lower temperatures, as in observations (e.g., Lin et al. 2003; McCarthy et al. 2007b), but  $f_{gas}$  is otherwise constant for  $T > 3$  keV. There is a hint of a weak separation between CC and NCC clusters with cool cores having somewhat higher gas fractions for a given temperature as we will discuss in Section 4.

The third panel presents a plot of gas mass out to  $r_{500}$  against  $T_{500SL}$ . There is a strong scaling relation with comparable power-law slopes for each type of cluster (measured slope index of  $1.61 \pm 0.04$  for CC clusters and  $1.69 \pm 0.01$  for NCC clusters). This scaling relation is qualitatively similar to that in Figure 11 from Chen et al. (2007), although the slope is a bit steeper than that observed and expected for self-similar behavior (Kaiser 1986) (i.e.,  $M \propto T^{1.5}$ ). Vikhlinin et al. (2006b) find a flatter slope for the  $M-T$  relation for their sample of 13 cool core clusters in comparison to other authors who analyzed mixed samples with CC and NCC clusters (and different techniques for measuring mass and temperature).

In a separate paper (Jeltema et al. 2007), we also show that the distribution of X-ray substructure within these clusters, as measured using power ratios, agrees with that observed from X-ray observations of nearby rich galaxy clusters.

Overall, within the noted limitations of these simulations, the average properties and the relationships between basic variables for the numerical clusters agree fairly well with X-ray observations.

#### 4. THE FORMATION OF CC AND NCC CLUSTERS

With a relatively large sample of numerical clusters, we are able to explore the question of why some clusters have cool cores but others do not. These simulations indicate that the evolution of CC clusters has followed a different history in terms of accretion of mass from the cosmic web in comparison to NCC clusters. Although each cluster has its own unique rich and complex evolutionary path

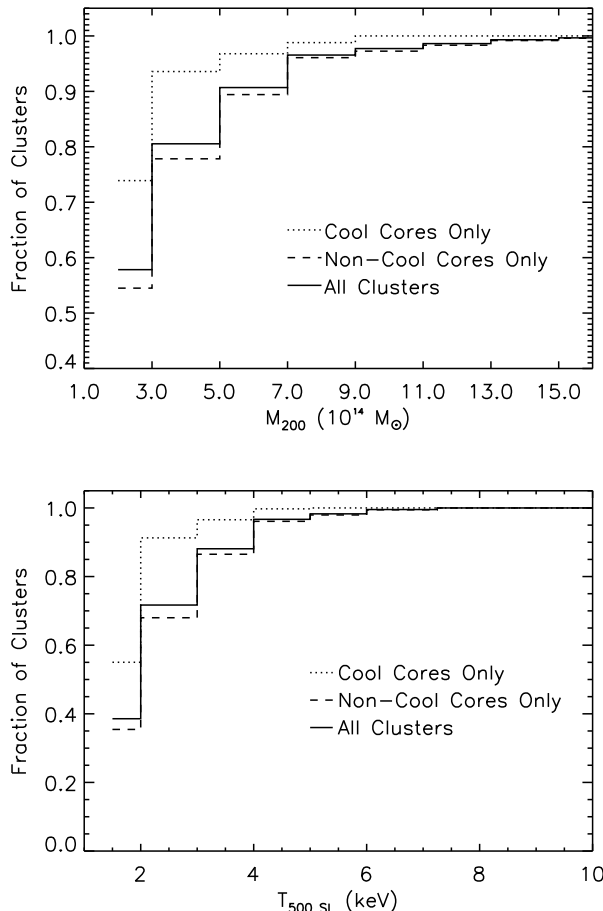


FIG. 2.— Distribution of the cumulative fractions of total cluster masses and  $T_{500SL}$  (spectroscopic-like temperatures within  $r_{500}$ ) for all clusters (solid) and for each cluster type in the catalog with  $M_{200} > 10^{14} M_{\odot}$  and  $z < 1$  (to approximately match present range of X-ray cluster observations).

that depends upon its initial mass and the density of surrounding halos, there are some clear general trends within this larger dispersion that we see which appear to separate CC from NCC clusters.

In Figure 4, we track the evolution of the median changes in cluster mass ( $M_{200}$ ) and the median central temperatures for the 10 most massive CC and NCC clusters from  $z = 0$  back to between  $z = 1$  and  $z = 2$  (each cluster is tracked back only to a time determined by our mass cutoff of  $M_{200} > 10^{14} M_{\odot}$ ). Although we use the ten highest masses in each sample for better statistics, we note that the same qualitative trends as shown in Figure 4, but with larger dispersion, are present for samples of CC and NCC clusters selected to have comparable mass distributions. We illustrate this evolution back to just  $z \approx 1.5$  because there are only a few CC clusters at  $z > 1.5$  above our  $10^{14} M_{\odot}$  mass limit (more clusters grow above this mass over time).

The two cluster types show different histories in their median mass accretion rates at early times. At  $z = 1.5$ , NCC clusters experience a median  $\approx 75\%$  change in mass per Gyr, albeit with a not unexpected large dispersion due to the wide range of merger states. The CC clusters have a median change of  $\approx 30\%$  in mass per Gyr with a smaller dispersion but also for fewer clusters with  $M_{200} >$

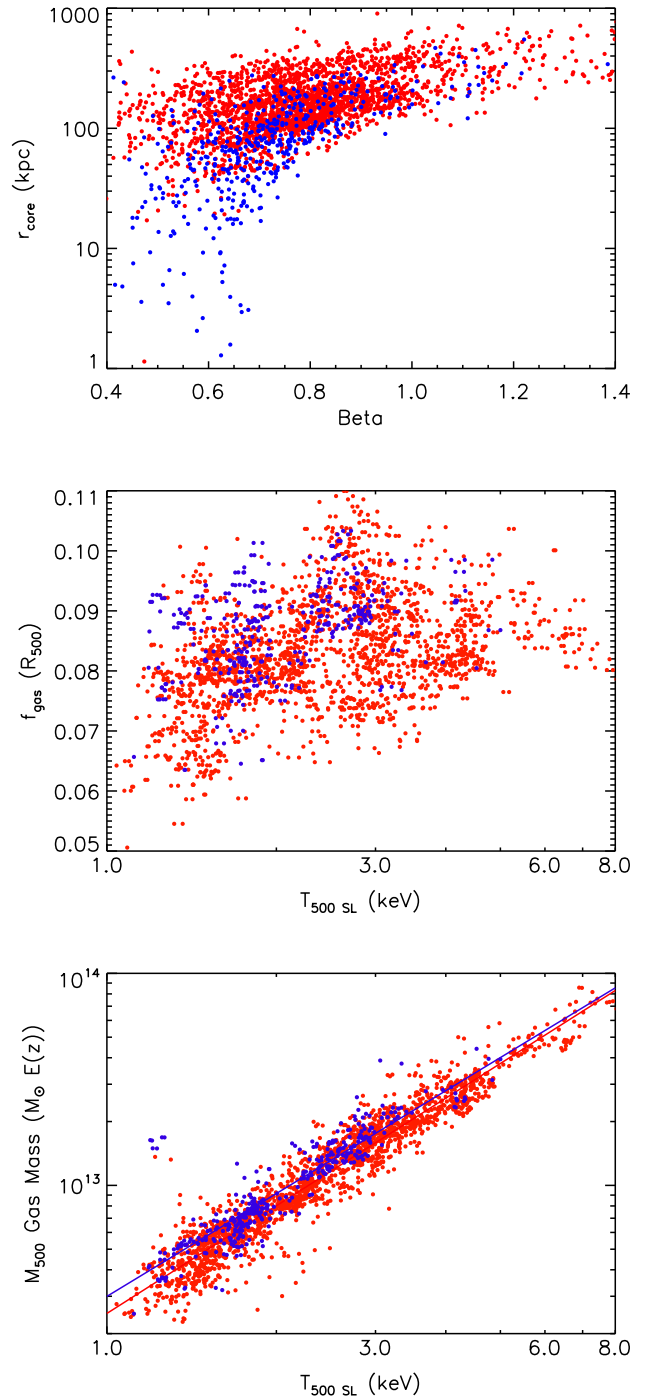


FIG. 3.— Statistical properties of numerical galaxy clusters with  $M_{200} > 10^{14} M_{\odot}$  and  $z < 1$ . Blue are CC and red are NCC clusters. Top:  $\beta$ -model fits to  $S_X$  profiles of individual clusters provide a measure of the core radius ( $r_{core}$ ) and slope ( $\beta$ ). Middle: Gas fraction versus  $T_{500SL}$  (spectroscopic-like temperatures within  $r_{500}$ ). Bottom: Gas mass out to  $r_{500}$  is plotted against  $T_{500SL}$ . Power-law fits, performed separately for CC and NCC clusters, are shown.

$10^{14} M_{\odot}$ . Using a K-S test, we find that for  $1 < z < 1.5$ , the distributions of mass change for NCC and CC clusters differ at the 95% level.

*The NCC clusters demonstrate a trend of experiencing major mergers early in their histories up to  $z \approx 0.5$ ,*

which destroy any initial cool cores, then they settle down to a more quiescent state thereafter. Here we define a “major” merger as one that has the potential for disrupting a nascent cool core, usually accreting  $\geq 50\%$  of the cluster’s previous mass over a timescale of  $\approx 1$  Gyr. *CC clusters, on the other hand, avoid mergers with high fractional mass changes early in their histories and instead grow slowly such that the cool cores increase in mass and stability.* As shown in Figure 4, CC clusters after  $z \approx 0.5$  have a relatively constant rate of accretion continuing to the present, similar to NCC clusters.

The central temperature plot in Figure 4 demonstrates that similar starting conditions can result in either CC or NCC clusters. At early epochs, the dispersion in central temperatures is large and the distributions are statistically indistinguishable between what will become CC and NCC clusters at  $z = 0$ . This contrasts to the significant difference in central temperatures between CC and NCC clusters for  $z < 0.5$ . Thus, the early merger history primarily determines the eventual cluster configuration at the present epoch.

In Figures 5 and 6, we show examples of the evolution of NCC and CC clusters, respectively, which well represent the general scenarios for how these clusters form. Our simulations indicate that lower mass clusters with  $T < 2$  keV form cool cores early in their history when initial conditions produce central densities and temperatures that allow the gas to radiatively cool. This suggests that many (most) lower mass clusters should have cool cores which is consistent with the data in Figure 8 in the next section and the observations of poor clusters composed of early-type galaxies (see e.g., review by Mulchaey 2004; Zabludoff & Mulchaey 1998; Ponman et al. 2003; Chen et al. 2007). According to our simulations, early mergers cause the fates of NCC and CC clusters to diverge.

As shown by the representative example in Figure 5, NCC clusters often undergo major mergers early in their history. This cluster had begun to develop a cool core at  $z = 1.25$  (see panel A). However, the cluster experienced a major merger (mass increased by  $\approx 100\%$ ) at  $z \approx 1$  and the cool core was greatly diminished (panel B). Smaller mass halos with cool cores continue to be accreted by this cluster but these CC’s are ram pressure stripped/disrupted usually within a single core passage (see panels C and D). By  $z \approx 0.65$ , there is no evidence of a CC associated with the cluster dark matter density peak at this or later times. Early mergers destroy the cool cores in NCC clusters, leaving behind hotter, thermalized, moderately dense cores where the cooling time is everywhere above the Hubble time. As shown in the next Section and in the Appendix, the NCC cluster gas has become mostly relaxed within the gravitational potential well (with minor perturbations from small infalling halos) with a surface brightness profile well represented by a  $\beta$ -model. Subsequently, cool halos infalling into these NCC clusters do not survive passage through the central parts of the clusters nor do the central conditions allow cool cores to re-establish. NCC clusters continue to experience minor mergers as they now slowly evolve (typically, mass increases only  $\approx 10\%$  over Gyr time frames after  $z \geq 0.5$  from multiple mergers for the NCC as shown in Figure 4). We suggest that such an early major merger produced the characteristics observed today for the NCC

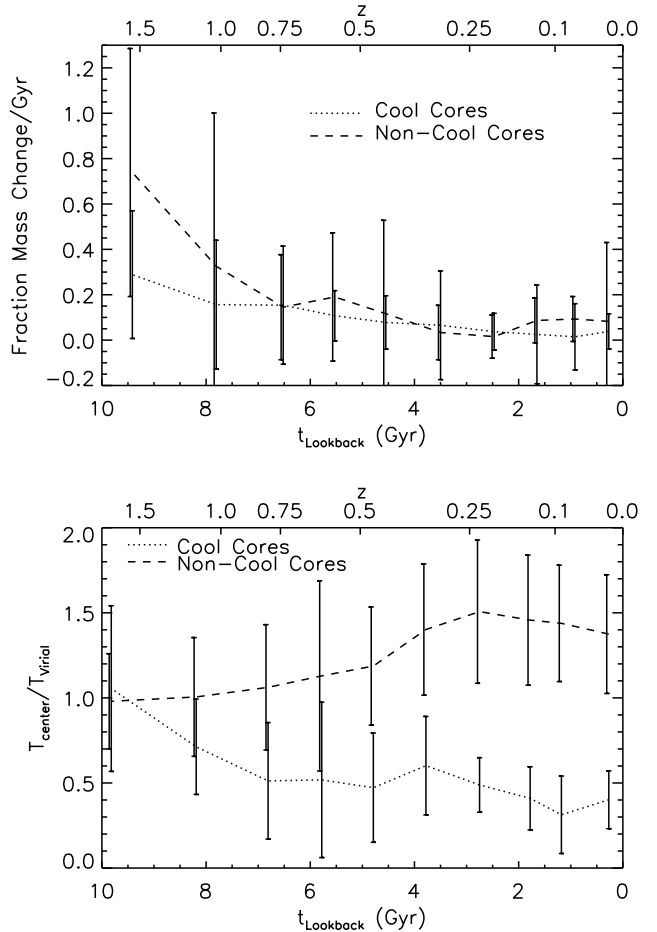


FIG. 4.— The median time evolution of the 10 most massive NCC clusters and the 10 most massive CC clusters. Dispersions in the distributions are also shown. Top: The median fractional mass change per Gyr as a function of lookback time and redshift. Bottom: Evolution of the median core temperatures (normalized by the virial temperature). The NCC clusters accrete significantly more mass than the CC clusters until  $z \approx 0.5$ , signifying more early major mergers than for the CC clusters. By  $z = 0.25$ , the core temperatures for the NCC clusters are about 3 times hotter than the CC clusters; the cool cores are well established and becoming more robust (slightly cooler and denser) throughout subsequent minor mergers. Coma cluster whose complex properties may be the result of previous mergers (Burns et al. 1994).

On the other hand, Figure 6 suggests that CC clusters evolve differently. This CC cluster had no significant change in mass until  $z = 0.75$  and its only major merger did not occur until  $z = 0.3$ . Figure 6 shows the temperature and central cool core as the merger is progressing (at  $z = 0.3$ ) (panel A). The next snapshot at  $z = 0.2$  shows the CC somewhat diminished but still present. The central temperature moved slightly upward but quickly readjusted downward as the CC easily survives the shock heating and ram pressure from the merger. In contrast to the simple cooling flow model, CC clusters may be no closer to hydrostatic equilibrium than NCC clusters with the equivalent mass (see also Section 5.5). This hierarchical formation model for CC clusters makes clear predictions of substructure and average cluster characteristics beyond the core that are testable with X-ray data.

Figure 7 shows the radial profiles of the baryon frac-

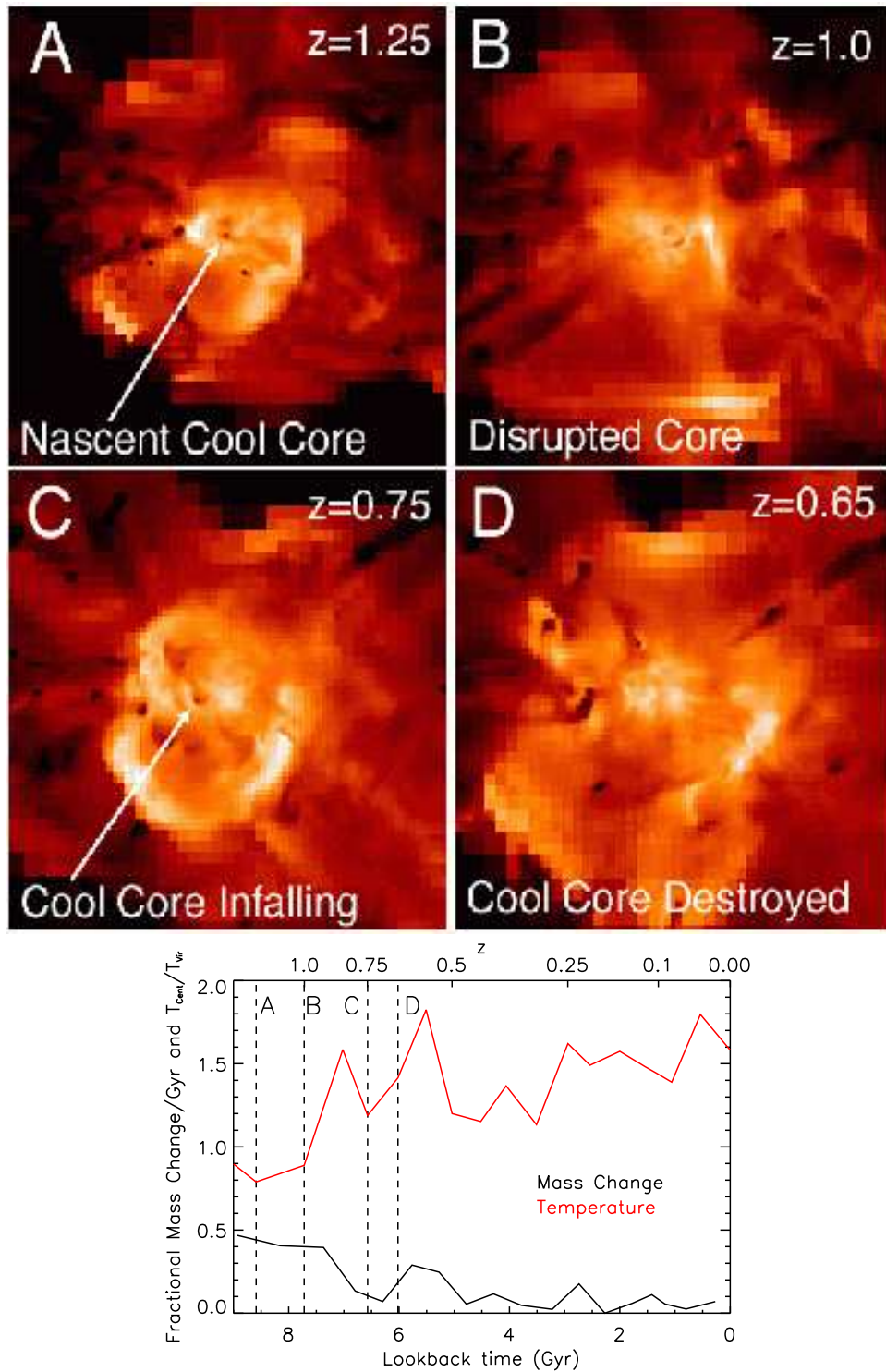


FIG. 5.— Four snapshots of the history of an NCC cluster with final ( $z = 0$ ) values of  $M_{200} = 8 \times 10^{14} M_{\odot}$  and  $T_{\text{virial}} = 5.5$  keV. Dashed vertical lines in the bottom panel correspond to different epochs of the temperature images.

tion and the temperature for representative examples of numerical CC and NCC clusters in our sample. Even outside of the cool core ( $\approx 0.05r_{200} \approx 100h^{-1}$  kpc, the first vertical dotted line), there is an excess of baryons relative to NCC clusters out to  $\approx 0.3r_{200}$  (second vertical dotted line). (We note that the dark matter density profiles are comparable for the CC and NCC clusters.) Such an extended “transition region” could be created, in part,

by gas “sloshing” in the cluster potential well following repeated mergers as proposed by Markevitch & Vikhlinin (2007).

Figure 7 also shows the temperature differences between each cluster type. The NCC cluster demonstrates the universal temperature profile that we described in Loken et al. (2002). The temperature profile of the CC cluster rises steeply to  $\approx 0.05r_{200}$  and then it has a

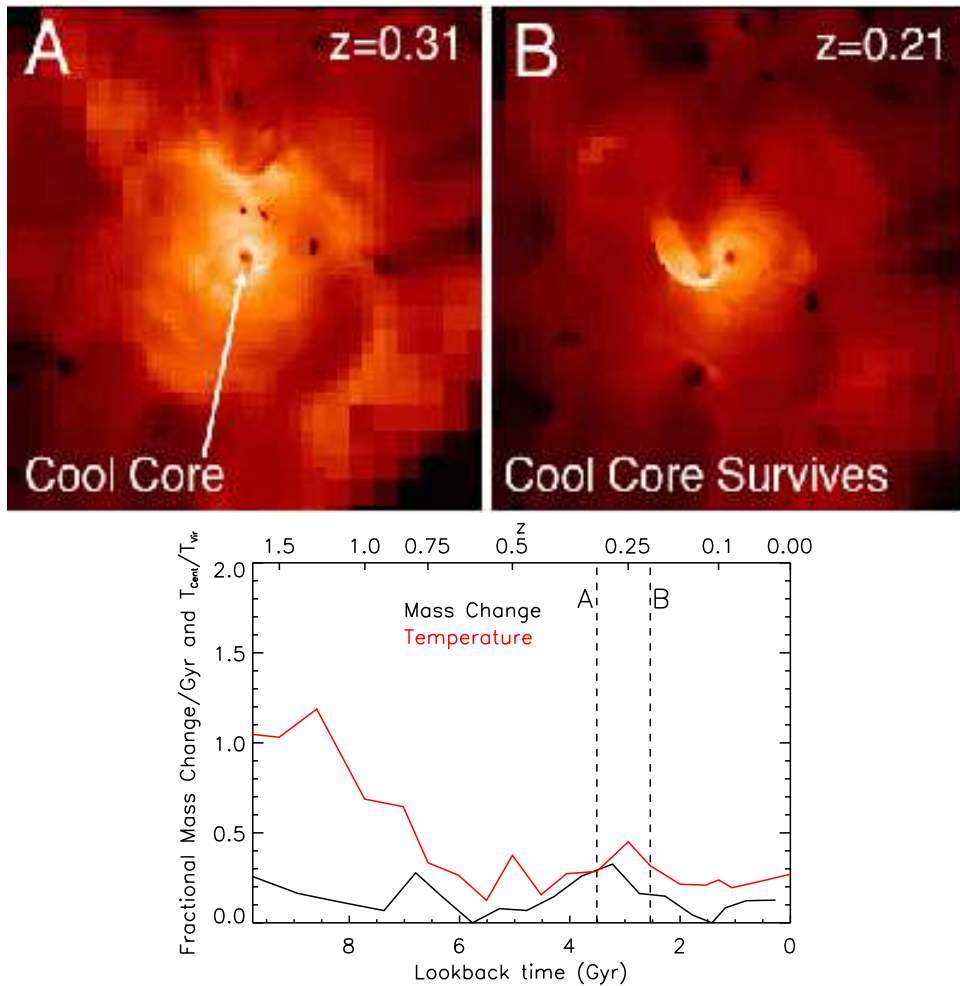


FIG. 6.— Two snapshots of the history of a CC cluster with  $M_{200} = 4.4 \times 10^{14} M_{\odot}$  and  $T_{\text{virial}} = 3.7$  keV at  $z = 0$ .

prolonged stretch of near-constant temperature, again within the region  $\approx 0.05r_{200}$  to  $\approx 0.3r_{200}$ . This CC cluster profile is less compact than that found for recent SPH simulations (Valdarnini 2006b) and agrees well with observations (see *e.g.*, Vikhlinin et al. 2006b; Baldi et al. 2007).

Using these two trends, we define three components to a cool core cluster: cool core, “transition region”, and outer region. The transition region is differentiated by the excess of baryons outside the core and relatively flat temperature profile (and low entropy) compared to NCC clusters. We have (subjectively) chosen the limits  $\approx 0.05r_{200}$  to  $\approx 0.3r_{200}$  for this transition region;  $\approx 0.05r_{200}$  is the traditional edge of the cool core where the slope of temperature changes dramatically, and  $\approx 0.3r_{200}$  is an average location where the baryon fraction of each type of cluster converges and the temperature begins to decrease. Most current cluster X-ray observations also measure  $S_X$  accurately out to only  $\approx 0.3r_{200}$ , meaning that most observations measure predominantly the transition region in CC clusters (as will be discussed further in Gantner et al. (2007)).

These simulations predict a very different set of cluster characteristics from those expected in the simple, non-evolving cooling flow model or from cooling-only simulations. Since CC and NCC clusters have experienced different magnitudes and epochs of mergers, there should

be observational signatures remaining from the mergers. In particular, we will show in the next section that the fraction of clusters with cool cores is expected to be strong function of the virial mass, in good agreement with recent observations. We then will show that single  $\beta$ -models systematically overestimate (or bias) the densities and masses beyond the cores in CC clusters. Furthermore, our simulations predict that more cool gas should be found beyond the cores in CC clusters in comparison to NCC clusters. Finally, this scenario forecasts that CC rich clusters should be found in denser super-cluster environments at the present epoch.

## 5. CONSEQUENCES OF EVOLUTIONARY DIFFERENCES IN CC AND NCC CLUSTERS

In this Section, we explore the differences in the properties of CC and NCC clusters based upon the results of our numerical simulations. The simulations predict substantial differences in the characteristics of these clusters beyond the cores. These predictions can be tested with data from current and planned X-ray telescopes.

### 5.1. Masses and Fractions of CC Clusters

An intriguing new result is that the fraction of clusters with cool cores is a strong function of cluster gas mass as shown in Figure 8. We display gas masses here

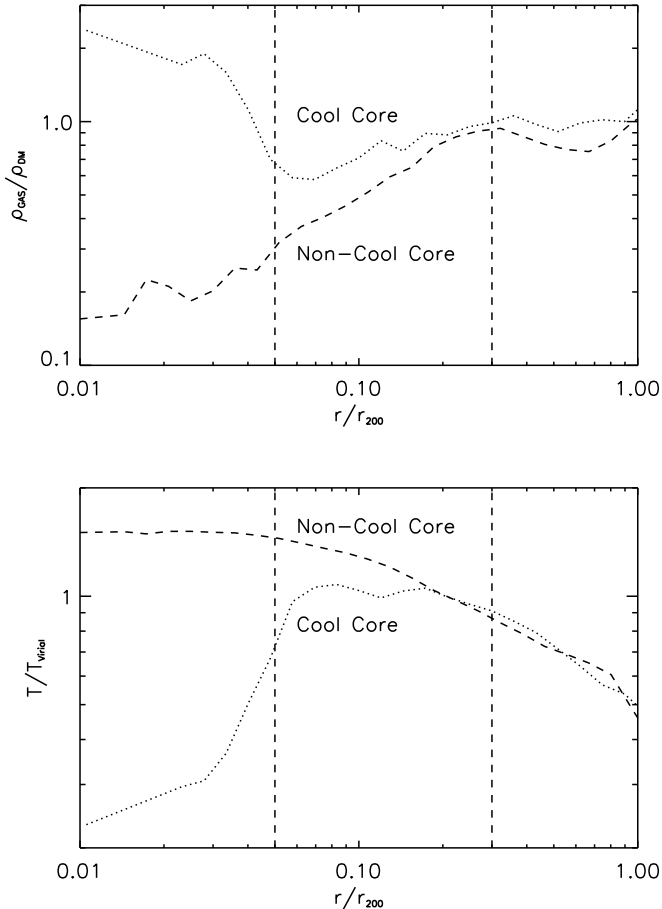


FIG. 7.— Plots of the gas fraction and temperature profiles for representative CC and NCC numerical clusters. The vertical lines designate the location of the newly defined CC cluster transition region ( $0.05r_{200}$  to  $0.3r_{200}$ ). This transition region contains an excess of baryons compared to a typical NCC cluster and a relatively flat temperature profile, indicating different gas properties than either the core or the outer region.

instead of total cluster masses to allow a direct comparison with the observation-derived data presented by O’Hara et al. (2006) and Chen et al. (2007). About a quarter of simulated clusters with  $M_{gas} \approx 5 \times 10^{12} M_{\odot}$  have cool cores whereas no high mass numerical clusters ( $M_{gas} > 4 \times 10^{13} M_{\odot}$ ) have cool cores. As a corollary to this result, we find that the mean total mass for the 10 most massive CC clusters at  $z = 0$  is  $2.4 \pm 1.4 \times 10^{14} M_{\odot}$  whereas the mean total mass for the 10 most massive NCC clusters is  $11.3 \pm 4.0 \times 10^{14} M_{\odot}$ . These results support the idea that cool cores are destroyed via multiple major mergers and the probability of cool core disruption increases as clusters grow to the size of the Coma cluster.

A similar result can be seen from observational samples of clusters using *ROSAT* data compiled by O’Hara et al. (2006) and by Chen et al. (2007). Both samples have a somewhat common ancestry from the work of Edge et al. (1990) with the samples consisting of nearby ( $0.01 < z < 0.1$ ), moderate X-ray luminosity clusters. In Figure 8, we have plotted data from O’Hara et al. (2006) and Chen et al. (2007) overlaid onto those for our sample of numerical clusters. Although the absolute values of the fractions differ between the observed and numer-

ical samples as discussed in Section 2, the general trend of decreasing fraction of CC clusters with mass is present for both observations and simulations.

This finding is contrary to the expectations of the simple non-evolving cooling flow model where the number of cool cores should increase with cluster mass (as the central gas density increases). Although observational selection effects are a possible concern in the O’Hara et al. (2006) and Chen et al. (2007) catalogs, we believe that this newly discovered trend contains important insights into the formation of CC versus NCC clusters.

### 5.2. Evolution in the Fraction of Cool Cores?

Recently, Vikhlinin et al. (2006a) reported that the number of observed CC clusters declines dramatically to 15% with redshift beyond  $z \approx 0.5$  (versus 65% for their nearby cluster comparison sample). Because of the limited spatial resolution with *Chandra* at these distances, they use the central slope or “cuspsiness of the surface brightness” to distinguish between CC and NCC clusters.

In Figure 9, we show the fraction within the co-moving volume of our numerical cool core clusters as a function of redshift for all clusters with  $M > 10^{14} M_{\odot}$  out to  $z \approx 1$ . The error bars in each bin reflect the  $\sqrt{N}$  uncertainties due to the number counts. Within these errors, the fraction of CC clusters is not a strong function of redshift out to  $z \approx 1$  (15-20%). For  $z > 1$ , the fraction drops to  $\approx 10\%$  but the dispersion is large because there are only a few CC clusters with  $M > 10^{14} M_{\odot}$  at these early epochs.

The flat distribution of CC fraction within the range  $0 < z < 1$  is not inconsistent with the evolutionary formation scenario described in Section 4 and shown in Figure 4 for several reasons. First, Figure 4 reveals that the greatest disparity in mass change between CC and NCC clusters occurs for  $z > 0.75$ . That is, most of the growth in NCC clusters via mergers occurs at the expense of CC clusters at earlier epochs. For  $z < 0.75$ , CC and NCC clusters grow at comparable rates. Second, although CC clusters continue to be lost via mergers for  $z < 0.75$ , this is counterbalanced by the fact that the numbers of CC clusters above the mass cutoff of  $10^{14} M_{\odot}$  continue to increase because CC clusters also grow via accretion. Thus, the rate at which CC clusters are destroyed is approximately equal to the rate at which new clusters are added above our  $10^{14} M_{\odot}$  mass limit. This produces the effect of no apparent evolution in the fraction of CC clusters for  $z < 1$  in a mass-limited sample.

In order to explain the Vikhlinin et al. (2006a) result within the context of our simulations, their sample would have to have substantial selection effects possibly driven by the unique choice of cool cores based upon the slope of the X-ray surface brightness profile and resolution effects. Alternatively, some form of time-dependent baryon physics (*e.g.*, higher feedback rates at earlier epochs as recently described by Eastman et al. (2007) for AGNs) not incorporated into the present simulations could potentially boost the fraction of CC clusters seen in the local Universe compared to earlier epochs.

### 5.3. Surface Brightness Profiles

Turning next to the large-scale X-ray surface brightness profiles ( $S_X$ ), we fit  $\beta$ -models in two different ways for two different subsamples of the numerical clusters to

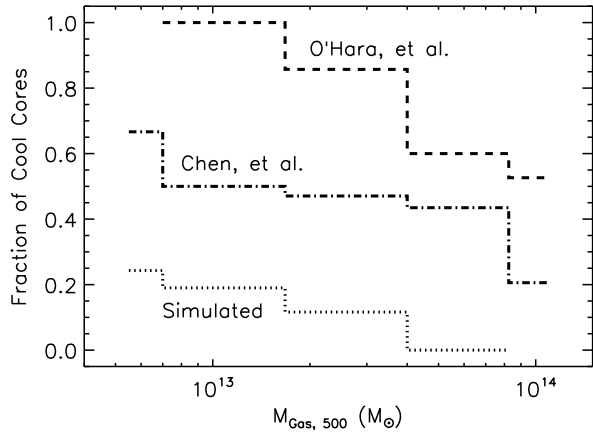


FIG. 8.— Fraction of all galaxy clusters with cool cores as a function of mass. The simulated data is from 1522 numerical clusters. Chen et al. (2007) is based upon their table of 106 observed clusters. O’Hara et al. (2006) is from their table of 45 observed clusters.  $M_{gas,500}$  was chosen as the measurement common across all three data sets. The differences in absolute fraction of CC clusters between the samples may have a variety of causes (*e.g.*, luminosity boosting by cool cores in flux-limited observational samples; numerical clusters may be affected by resolution effects, selection of cosmological parameters, or feedback prescription).

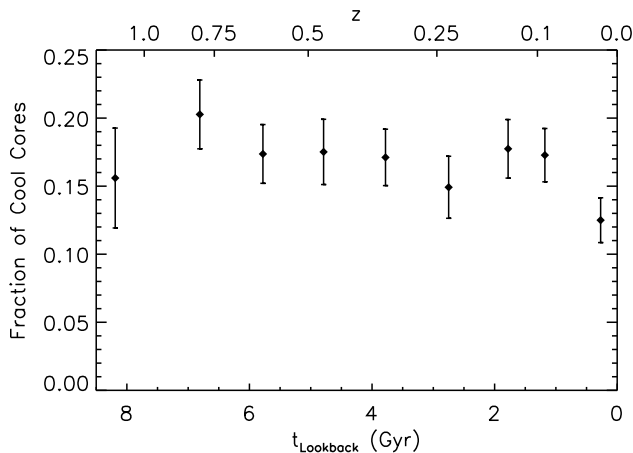


FIG. 9.— Fraction of cool cores as a function of redshift for numerical clusters. In contrast to Vikhlinin et al. (2006a), we find no change in the fraction of cool cores with redshift.

examine potential differences in the shapes and core radii of CC versus NCC clusters.

We began by producing average  $S_X$  profiles from projected X-ray images along a single axis for all the clusters at  $z = 0$  and with  $M > 10^{14} M_\odot$ , separated into CC (10 clusters) and NCC (78 clusters) categories (several  $z = 0$  clusters were not used because of contamination by multiple clusters). The flux for individual profiles was first normalized by  $M_{200}^{3/2}$  (from the Mass-Temperature scaling relationship as in Finoguenov et al. (2001)) before averaging them together. We then fit a  $\beta$ -model to each of these average profiles as would be done for observations. That is, we fit the profiles out to  $0.3r_{200}$  (roughly corresponding to  $0.5r_{500} \approx 0.5$  Mpc) which is the typical limit to the observed surface brightness in most X-ray exposures with current instruments (as we discuss further

in Gantner et al. (2007)). For the average CC profile, we excluded the cool core in making the  $\beta$ -model fit. The result is shown in Figure 10.

This figure indicates that the profiles (beyond the cool core) for CC clusters are distinguished from NCC clusters in several important ways. First, the parameters for the  $\beta$ -models are different. For the average CC profile,  $r_c = 0.05 \pm 0.09 r_{200}$  and  $\beta = 0.66 \pm 0.12$ , whereas for the NCC average  $S_X$  profile,  $r_c = 0.12 \pm 0.02 r_{200}$  and  $\beta = 0.66 \pm 0.07$ . That is, the cluster core radii are much smaller for CC clusters, as also shown in Figure 3. There is also considerably more scatter in the fit for the CC average profile (consistent with more variation between individual profiles) than for the NCC  $S_X$  profile. Second, the shape of the two  $S_X$  profiles are different within the transition region where the slope of the NCC is generally flatter than the CC cluster, as would be expected from Figure 7. There are similar slope differences in the  $S_X$  profiles between the NCC (Abell 401) and CC (Abell 85) clusters computed from deep Chandra observations reported by Vikhlinin et al. (2006b). Third, the  $\beta$ -model is a better fit to the average NCC cluster profile than to the CC profile. In particular, the  $\beta$ -model fit to the regions that would be typically observed by current satellites (*i.e.*, the transition region) for CC clusters significantly overshoots the actual flux in the outer parts of clusters. At  $r_{200}$ , the  $\beta$ -model overestimates the flux of the average CC profile by a factor of 3.8. This will result in a serious bias of cluster gas masses as we discussed in Hallman et al. (2006).

We also fit  $\beta$ -models to individual profiles for all numerical CC and NCC clusters (from a single projection) in our master database with  $M > 5 \times 10^{14} M_\odot$  and  $z < 2$ . In this case, we fit models out to  $r = r_{500}$ . We did not use the inner portion of the profiles dominated by the cool core (determined by the point where the slope of the temperature profile becomes negative) in making fits to CC clusters. We then calculated the reduced  $\chi^2$  goodness-of-fit values (including extrapolations of the fits out to  $r_{200}$ ) as compared with the numerical X-ray profiles. A histogram of those reduced  $\chi^2$  values for CC and NCC clusters is shown in Figure 11. As also indicated in Figure 10, the  $\beta$ -models fit the NCC clusters much better than the CC clusters. About 88% of the NCC clusters have  $\chi^2 < 1$ , whereas about one-third of the CC clusters have  $\chi^2 > 1$ . Once again, this is caused by the slope changes from the transition region to the outer core in the CC clusters which is not fit well by a single  $\beta$ -model.

As we show in the Appendix, good  $\beta$ -model fits to  $S_X$  suggest that a nonisothermal gas in the intracluster medium (ICM) is in approximate (but not necessarily perfect, see Section 5.5) equilibrium with the gravitational potential well of the cluster (under the assumption that the ICM gas is polytropic). So, the above results suggest that the ICM in NCC clusters is approximated by a gas with a balance between heating and cooling that is quasi-relaxed in an NFW-like dark matter potential. This is consistent with Figure 4 which shows that NCC clusters underwent major mergers early in their history but have subsequently settled into a quasi-equilibrium state with only minor on-going mergers. This contrasts with CC clusters that have temperature and density profiles inconsistent with a simple adiabatic gas well beyond

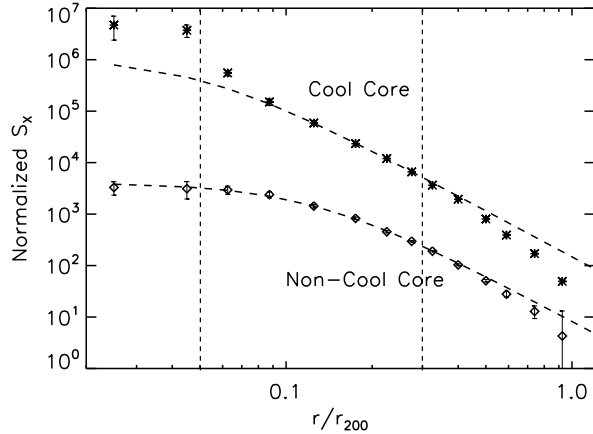


FIG. 10.— Average synthetic X-ray surface brightness profiles for CC and NCC clusters with  $z = 0$  and  $M > 10^{14} M_{\odot}$  (10 CC averaged together and 78 NCC averaged together). Error bars are errors on the mean determined from variations within each bin. Dashed curves are the best fit  $\beta$ -models within the “transition region” (*i.e.*, between the vertical lines from  $0.05r_{200}$  to  $0.3r_{200}$ ) for the CC average cluster profile and the best fit including all the points out to the right-most vertical line for the NCC cluster profile. The NCC profile was arbitrarily shifted downward by a factor of 10 to better distinguish it from the CC profile.

the cool core.

Vikhlinin et al. (2006b) recently analyzed the gas and total mass profiles for 13 nearby, “relaxed” clusters with temperatures between 0.7 and 9 keV using data from *Chandra*. All of the clusters in this sample have cool cores. They examined the surface brightness profiles out to at least  $r_{500}$  and concluded that the profiles are “not described well by a beta model”. When single  $\beta$ -models are fit to the inner portions of the clusters (but excluding the cool cores), they poorly extrapolate the gas density and mass profiles in the outer parts of the CC clusters as we found for the numerical clusters. In addition, Vikhlinin et al. (2006b) observed that the cooler regions in low temperature clusters are confined to a smaller fraction of the virial radius than in the hotter CC clusters. This is consistent with trends found in our numerical simulations as described by Hallman et al. (2006) and by Akahori & Masai (2006). Finally, Vikhlinin et al. note that low temperature (mass) clusters ( $T < 2.5$  keV) with cool cores have a bigger ratio of central to virial temperature than do the clusters with larger  $T_{virial}$ . We plan to explore the origin of this effect with new higher resolution simulations with more sophisticated heating prescriptions.

#### 5.4. Temperatures and Hardness Ratios Beyond the Cluster Cores

The temperature profiles for the two clusters shown in Figure 7 indicate that the temperature distributions for CC and NCC clusters are substantially different out to  $\approx 0.3r_{200}$ . In particular, the broad “transition region” has both a cooler and flatter distribution of temperature outside the cool core for the CC cluster in comparison to the NCC cluster. How general is this result for the total sample of numerical clusters? To address this question, we made emission-weighted temperature images of the clusters in our numerical cluster catalog with  $M_{200} > 5 \times 10^{14} M_{\odot}$  and  $0 < z < 0.5$ . From these images, we

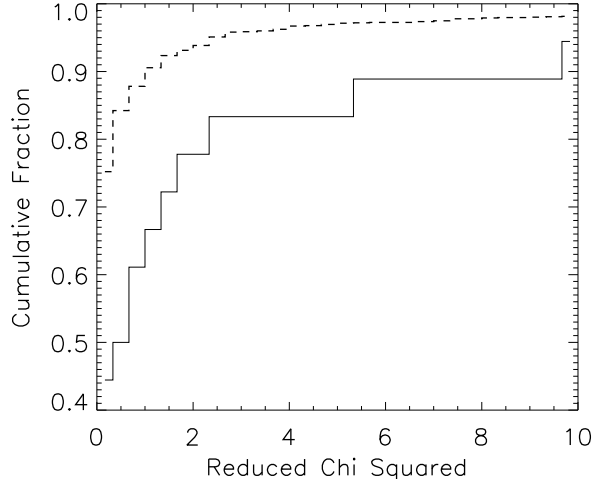


FIG. 11.— Histograms of the reduced  $\chi^2$  values for  $\beta$ -model fits for CC (solid) and NCC (dashed) clusters. Each numerical cluster ( $M_{200} > 5 \times 10^{14} M_{\odot}$ ,  $z < 2$ ) is fit to  $r_{500}$  and extrapolated out to  $r_{200}$ , and a  $\chi^2$  goodness-of-fit is calculated for the entire profile.

produced the histogram of temperatures (normalized by  $T_{virial}$ ), excluding cool cores, shown in Figure 12. The distribution of temperatures beyond the cool cores for CC clusters is significantly different from NCC clusters with a broad tail toward lower temperatures. CC clusters have  $\sim 40\%$  more gas with  $T_{ew} < 0.3T_{virial}$  beyond the cores than NCC clusters.

We predict that this signature will be apparent in hardness ratio maps that are commonly made from X-ray observations. As shown in Figure 13 for four typical cases drawn randomly from our simulations, the hard-to-soft band ratios (2-8 keV/0.5-2 keV) do a good job of illustrating the abundance of cooler gas beyond the cores in CC clusters. Figure 14 shows the cumulative fraction of pixels below a given hardness ratio for all four clusters in Figure 13. For the two CC clusters, we have excised the cool cores ( $< 0.05r_{200}$ ) so as not to bias the results with gas already known to be cooler than its NCC counterpart. As expected, the two CC clusters have a majority of pixels with values  $< 1$  and therefore are cooler in the transition region than the NCC clusters. The NCC clusters are both centered approximately at hardness ratio  $\approx 1$ , hence the gas in these clusters is roughly at the virial temperature of the clusters.

We shall show in Gantner et al. (2007) that there is very good agreement in the predicted hardness ratios from our simulations with X-ray observations of clusters from the *Chandra* and *ROSAT* archives.

#### 5.5. The Supercluster Environments of CC and NCC Clusters

The mass and temperature evolution plots in Figure 4 indicate that NCC clusters underwent major mergers early in their history in contrast to the milder accretion over time for CC clusters. This may also suggest that the larger scale environments in which these two types of clusters live are different since accretion of halos and diffuse material must come from the cosmic web. It is possible that NCC clusters began their lives in higher overdensity regions which then accelerated the growth of

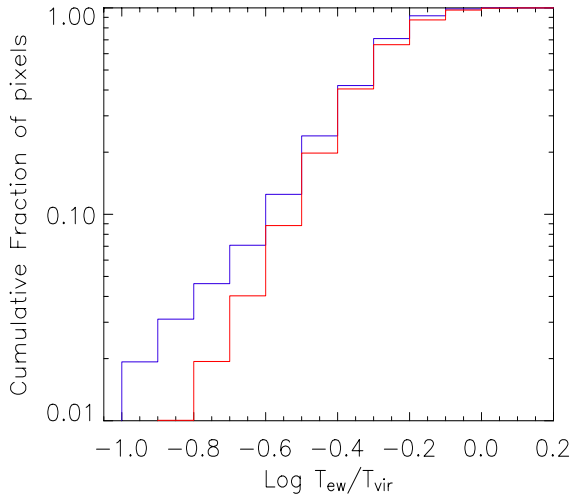


FIG. 12.— Histograms of the ratio of emission-weighted temperatures ( $T_{ew}$ ) from  $r = 180h^{-1}$  kpc to  $r_{200}$  divided by  $T_{virial}$  from temperature images for CC and NCC clusters. Clusters from the numerical catalog are included with  $M_{200} > 5 \times 10^{14} M_{\odot}$ . Red are NCC and blue are CC clusters.

these clusters via mergers (see *e.g.*, Mo & White 1996; Gao et al. 2005).

In an effort to explore the possible influence of the differences in the supercluster environments for CC and NCC clusters, we calculated the real space densities (which are expected to correlate with accretion rates) of all halos with  $M_{200} > 10^{13} M_{\odot}$  ( $\approx$  mass resolution of simulations) within a radius of  $5r_{200}$  of numerical rich clusters with virial masses  $1 - 6 \times 10^{14} M_{\odot}$  (approximate mass range of the CC clusters as shown in Figure 2). We calculated these densities for a series of redshifts between 0 and 1.5, and separated clusters by CC and NCC according to our definitions in Section 2.

The ratio of supercluster densities for CC to NCC clusters as a function of redshift is shown in Figure 15. At early epochs ( $z > 1$ ), the average supercluster density is somewhat higher around NCC clusters than CC clusters. One might expect clusters that are experiencing major bouts of accretion of subclusters that result in the destruction of embryonic cool cores to be surrounded by a higher density of halos. At times corresponding to  $0.7 < z < 1$ , there may a slight underdensity of halos around NCC clusters in comparison to CC clusters as one might expect if the NCC clusters suffered a large amount of mass accretion effectively “clearing out” its nearby neighborhood. Interestingly, at late times ( $z < 0.3$ ), the density of halos around CC clusters is  $\approx 30\%$  greater than for NCC clusters. However, unlike earlier epochs where the mass ratio of the main cluster to the average neighboring cluster is often  $\approx$  a few, this average mass ratio of the rich cluster to the halos at  $z < 0.3$  is much larger as the main cluster has grown considerably over the past 10 Gyr. This means that there are many small subclusters falling into the CC clusters but their relative impact is small compared to that for NCC clusters at earlier epochs

(see Figure 7). However, the above trends are weak at best and there is a large dispersion in supercluster densities between individual clusters.

It is interesting to note that this possible trend of overabundance of halos around numerical CC clusters at the present epoch is also found in Abell clusters. Loken et al. (1999) constructed a volume-limited sample of  $z < 0.1$  Abell clusters that was estimated to be 98% complete in an effort to investigate their supercluster environs. They separated clusters into CC and NCC. They found that CC Abell clusters have twice the density of neighboring clusters as do NCC clusters out to a radius of  $43 h^{-1}$  Mpc. We attempted to mimic the Loken et al. (1999) analysis by recomputing halo densities out to radii of  $43 h^{-1}$  Mpc and included neighbor halos in the calculation only if they had masses  $> 10^{14} M_{\odot}$  (*i.e.*, Abell-like clusters). We found that the density of neighboring halos is  $\approx 40\%$  greater for CC than NCC clusters, slightly larger than in Figure 15, but still considerably less than what Loken et al. (1999) propose for Abell clusters.

### 5.6. Deviations from Hydrostatic Equilibrium

Galaxy clusters are potentially powerful tools for precision cosmology. Accurate cluster mass determinations and gas fractions, along with cluster abundance counts, can provide key constraints on the dark energy parameter,  $w$ , as well as  $\Omega_b$ ,  $\Omega_m$ , and  $\sigma_8$  (*e.g.*, Wang & Steinhardt 1998; Haiman et al. 2001). In recent efforts, samples of CC clusters are being used exclusively because they are believed to be dynamically relaxed. For example, Allen et al. (2007) selected a sample of 42 hot, X-ray luminous clusters with  $0.05 < z < 1.1$ , all of which have short central cooling times ( $<$  a few  $10^9$  yrs), to constrain cosmological parameters from  $f_{gas}$ . Previous simulations (*e.g.*, Rasia et al. 2006; Nagai et al. 2007, and references therein) have called into question hydrostatic equilibrium for clusters. But, are CC clusters really more dynamically relaxed than NCC clusters? Figures 4 and 15 seem to call this assumption into question.

To explore this further, we calculated the deviations from hydrostatic equilibrium for all the clusters in our numerical archive with  $M_{200} > 10^{14} M_{\odot}$  (see also Jeltama et al. 2007). We did this by calculating the estimated mass of clusters from the gradients in the temperatures and gas densities in the usual way assuming hydrostatic equilibrium. In this case, we have used the spherically averaged profiles of temperature and density from the three-dimensional simulated cluster data. We have therefore eliminated any systematic effect resulting from conversion of observed quantities. So we expect that the resulting “hydrostatic masses” should be closer to the true values than ones which would be observationally derived. We then compared these hydrostatic masses to the true mass for each cluster. We did this for a series of redshift intervals between 0.0 and 1.5, and separated clusters between CC and NCC. The result is shown in Figure 16.

The average estimated cluster masses assuming hydrostatic equilibrium are biased low for all the clusters by  $\approx 15\%$ . This bias is constant for CC clusters at different redshifts but appears to be slightly worse for NCC clusters at earlier epochs ( $\approx 19\%$ ). In addition to the bias, the scatter in these mass estimates is high. 20% to

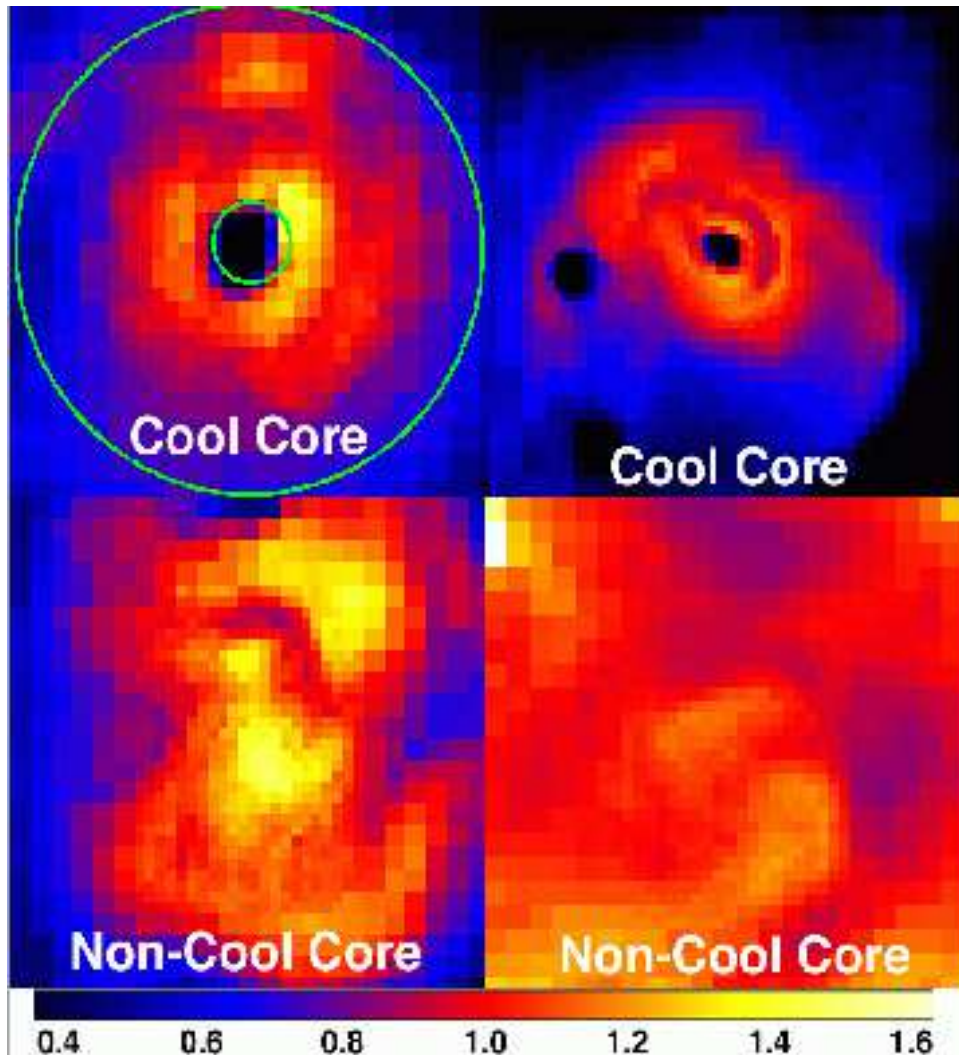


FIG. 13.— A sample of X-ray hardness ratio (HR) maps from 4 different simulated clusters (2 CC on top and 2 NCC on bottom) with fields of view of  $0.33r_{200}$ . The two circles in the upper left image delineate the “transition region” between  $0.05r_{200}$  to  $0.3r_{200}$  as described in Figure 7. Each HR map was made by dividing an image of the X-ray surface brightness from 2 to 8 keV by an image from 0.5 to 2.0 keV (i.e., typical *Chandra* hard and soft bands). Each is then normalized by the hardness ratio corresponding to the cluster virial temperature so that values  $< 1$  represent gas with  $T < T_{\text{virial}}$ . Note that non-central cool “blobs” are generally infalling halos.

30% underestimates are possible at the  $1\sigma$  level. Importantly, and what is new here, CC clusters are no better than NCC clusters as biased mass indicators. Both are equally low, although the scatter in CC clusters is about half that of the NCC clusters.

Markevitch & Vikhlinin (2007) similarly cast doubt on hydrostatic equilibrium in CC clusters due to the common presence of observed cold fronts and the inferred “gas sloshing”. For the clusters in our simulations, we find that the kinetic energy of bulk gas motions contributes at the  $\approx 10\%$  level compared to the total energy (see also Rasia et al. 2006).

If our numerical clusters are representative of real clusters, the apparent significant deviations from hydrostatic equilibrium for both CC and NCC clusters must be considered in choosing to use them for precision cosmology estimators.

## 6. SUMMARY AND CONCLUSIONS

Galaxy clusters are complicated, generally non-equilibrium systems where nongravitational physics is important in the cores. To the best of our knowledge, no

previous numerical simulations have been able to produce both cool core (CC) and non-cool core (NCC) clusters in the same numerical volume. Our heating and cooling prescription (with an approximate balance between heating and cooling), however, has resulted in a simulation with both CC and NCC clusters. The temperature profiles of our numerical CC clusters qualitatively match observations, although the central gas densities are higher than observed. Our fraction of cool cores is low compared to that of recent observed samples. On the other hand, the distinction in  $\beta$ -model parameters ( $r_c$  and  $\beta$ ) between CC and NCC clusters observed in samples of real clusters is reflected in our numerical clusters. Similarly, the distributions of gas fraction and gas mass with emission-weighted projected temperatures agree fairly well with observations. Overall, our numerical clusters have general characteristics that concur with X-ray data of observed clusters.

We propose an answer to the question posed in the title of this paper, *i.e.*, only some clusters have cool cores because of evolutionary differences driven by early major mergers. Our numerical simulations suggest that the his-

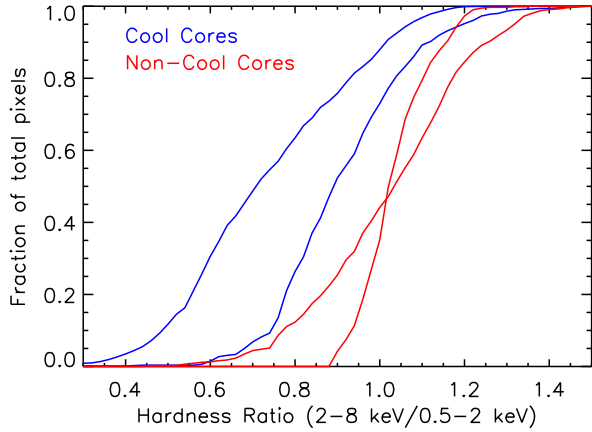


FIG. 14.— The cumulative fraction of pixels below each hardness ratio value for the sample of simulated clusters in Figure 13. The plot was assembled for regions between  $0.05-0.3r_{200}$  (excludes cool core in CC clusters). The NCC clusters are centered roughly at 1, meaning that most of their gas is approximately equal to  $T_{virial}$ . The CC clusters are noticeably cooler in this transition region.

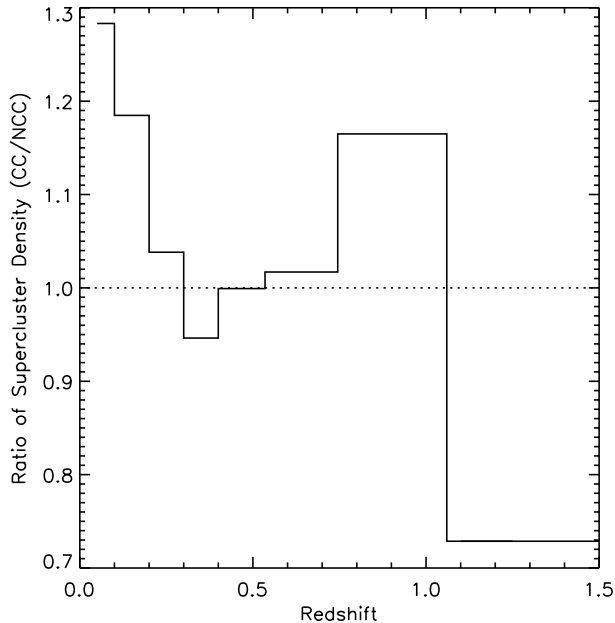


FIG. 15.— Histograms of the ratio of the real space densities of halos surrounding numerical clusters with  $M_{200} = 1 - 6 \times 10^{14} M_{\odot}$  for CC versus NCC clusters.

tories of cool core and non-cool core clusters are significantly different. Our NCC numerical clusters suffer early major mergers when nascent cool cores are destroyed. CC clusters, on the other hand, grow more slowly without early major mergers. CC clusters have a broad “transition region” in their gas distribution extending between the cool core and a radius of  $\approx 0.3r_{200}$  where the gas fraction is higher than for NCC clusters and the temperature profile is nearly isothermal. This transition region and difference in evolution lead to a number of testable predictions for X-ray observations of real clusters.

We find that the fraction of cool core clusters is a

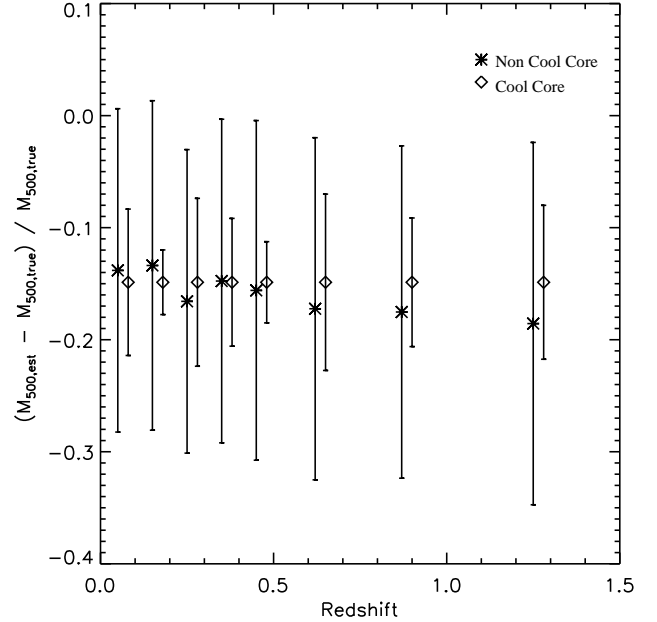


FIG. 16.— The fractional deviation of cluster masses estimated assuming hydrostatic equilibrium versus the true virial masses as a function of redshift. The standard deviations in the distributions are also shown.

strong function of mass with fewer CC clusters at higher gas masses. This general trend qualitatively agrees with the analysis of recent nearby X-ray cluster samples by O’Hara et al. (2006) and Chen et al. (2007). On the other hand, we do not find any significant variation in the fraction of numerical cool cores with redshift in contrast to the recent claim by Vikhlinin et al. (2006a).

The X-ray surface brightness profiles for NCC clusters are well fit by single  $\beta$ -models whereas the outer emission for CC clusters is biased low compared to  $\beta$ -models. The resulting gas densities and gas masses of CC clusters estimated from single  $\beta$ -model extrapolations are biased high by factors of 3-4.

CC clusters have  $\approx 40\%$  more cool gas beyond the cores within the transition region than do NCC clusters. This results in a very different distribution of X-ray hardness ratios beyond the cool core for CC versus NCC clusters. We predict that such differences will be observable with current X-ray imagers.

There are some indications that the supercluster environs for CC and NCC clusters are different from each other today and in past epochs. At  $z > 1$ , NCC clusters appear to have more halos in their neighborhoods than CC clusters. At  $z < 0.3$ , this trend is reversed with more halos around CC clusters. This separation between CC and NCC clusters for low  $z$  clusters qualitatively agrees with supercluster density calculations for nearby Abell clusters.

Finally, we find that both CC and NCC clusters are biased low in their mass estimation by  $\approx 15\%$  assuming hydrostatic equilibrium. In this sense, it appears that CC clusters are no better than NCC clusters as mass estimators, unlike what is generally assumed. This is important to consider in using CC clusters for precision estimations of cosmological parameters.

In an upcoming paper (Gantner et al. 2007), we will

compare the above predictions with X-ray observations of rich clusters from both the *Chandra* and *ROSAT* archives. The initial agreement is quite good.

There are some important remaining issues with the current simulations. We plan to address these with a series of new numerical simulations at higher resolution to overcome the limitations of the current computational set of clusters. We will explore the impact of  $\Omega_b$  and  $\sigma_8$  on the fraction of cool cores that are produced in the computational volume. We will also refine our heating/cooling prescription to better match current observational constraints. Once the influence of these factors is understood on the creation of CC and NCC clusters, the fraction of cool core clusters could serve as an important new con-

straint on cluster baryonic physics and/or dark energy models.

This work was supported in part by grants from the National Science Foundation (AST-0407368) and the NASA ADP (NNX07AH53G) program. We thank Brian O'Shea, T. Reiprich, M. Voit, and M. Markevitch for stimulating discussions. We acknowledge the referee for providing useful comments and suggestions. We also appreciate the Aspen Center for Physics for hosting several of the authors (JOB, EJH) where some of the final work on this project was completed.

## APPENDIX

### APPENDIX: X-RAY PROFILE FOR AN ADIABATIC ICM IN AN NFW CLUSTER POTENTIAL

What does a good fit to the X-ray surface brightness profile by a  $\beta$ -model imply about the dynamical state of the cluster gas when it is nonisothermal? When the intracluster gas is relaxed in a Navarro et al. (1997) (NFW) dark matter potential (derived from N-body simulations) and in hydrostatic equilibrium, we can solve a simple equation for its radial distribution (see also Navarro et al. 1997; Makino & Asano 1999). The equation for hydrostatic equilibrium is a simplification of the Euler equations for an ideal fluid, setting fluid velocity to zero gives

$$\nabla P_{gas} = -\rho_{gas}g, \quad (A1)$$

where  $P_{gas}$  is the pressure of the ICM gas,  $\rho_{gas}$  indicates the gas density, and  $g$  is the local gravitational acceleration. Under the assumption of spherical symmetry, we can simplify this to

$$\frac{dP_{gas}}{dr} = -\rho_{gas}(r)g(r). \quad (A2)$$

We assume here that the dark matter potential dominates the gravitation, and do not include the contribution of the gas to the potential, which should result in only minor error. In that case, we can write  $g(r)$  from an NFW dark matter profile as

$$g(r) = \frac{GM_{<R}}{r^2}, \quad (A3)$$

where  $G$  represents the universal gravitational constant, and  $M_{<R}$  indicates the dark matter mass inside the radius of interest. That mass can be calculated by integrating the NFW profile

$$\rho_{dm}(x) = \rho_{0,dm} \frac{1}{x(1+x)^2} \quad (A4)$$

where

$$x = \frac{r}{r_c} \quad (A5)$$

and  $r_c$  is the core radius and  $\rho_{0,dm}$  is the central normalization of the profile. Integrating the profile to get the total enclosed mass

$$M_{<R} = 4\pi r_c^3 \rho_{0,dm} \int \frac{1}{x(1+x)^2} x^2 dx \quad (A6)$$

We assume that the gas follows a nonisothermal, adiabatic equation of state such that

$$P = k\rho^\gamma. \quad (A7)$$

where  $k$  is a constant. Then, the hydrostatic equilibrium equation to be solved can be written as

$$\frac{dP_{gas}}{dr} = -P^{1/\gamma} \frac{4\pi G r_c^3 \rho_{0,dm}}{r^2} \left[ \int \frac{1}{x(1+x)^2} x^2 dx \right]. \quad (A8)$$

Numerical integration of Eq. 8 results in the profiles shown in Figure 17. The solid line is the solution to Eq. 8, the dashed is the NFW dark matter density profile, and the dotted is a standard  $\beta$ -model fit to the gas density. Note that the  $\beta$ -model fits Eq. 8 very well for  $r > 0.2r_c$  but the  $\beta$ -profile is somewhat flatter in slope within the core in comparison to Eq. 8. This suggests that good  $\beta$ -model fits to X-ray profiles imply gas that is relatively relaxed within the dark matter potential.

## REFERENCES

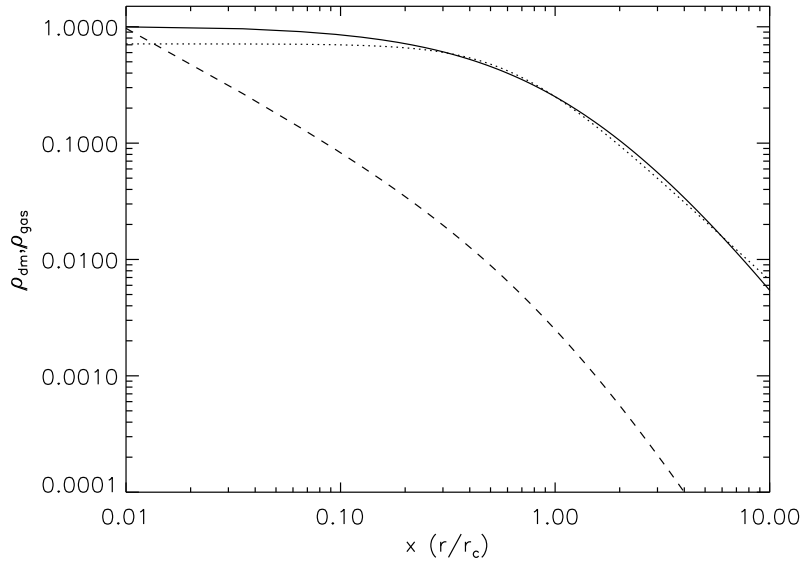


FIG. 17.— Density profiles described in the text. Dashed is the standard NFW dark matter density profile in arbitrary units, solid line is the resulting gas density profile from integrating the equation of hydrostatic equilibrium in the NFW potential. The dotted line is a standard  $\beta$ -model fit to the gas density profile.

- Baldi, A., Ettori, S., Mazzotta, P., Tozzi, P. & Borgani, S. 2007, *ApJ*, 666, 835
- Brickhouse, N. S., Raymond, J. C., & Smith, B. W. 1995, *ApJS*, 97, 551
- Brüggen, M. & Kaiser, C. R. 2002, *Nature*, 418, 301
- Burns, J. O. 1990, *AJ*, 99, 14
- . 1998, *Science*, 280, 400
- Burns, J. O., Loken, C., Gomez, P., Rizza, E., Bliton, M., & Ledlow, M. 1997, in *ASP Conf. Ser. 115: Galactic Cluster Cooling Flows*, ed. N. Soker, 21
- Burns, J. O., Motl, P. M., Norman, M. L., & Bryan, G. L. 2004, in *The Riddle of Cooling Flows in Galaxies and Clusters of galaxies*, ed. T. Reiprich, J. Kempner, & N. Soker, 291
- Burns, J. O., Roettiger, K., Ledlow, M., & Klypin, A. 1994, *ApJ*, 427, L87
- Cen, R. & Ostriker, J. 1992, *ApJ*, 393, 22
- Chen, Y., Reiprich, T. H., Böhringer, H., Ikebe, Y., & Zhang, Y.-Y. 2007, *A&A*, 466, 805
- Donahue, M. & Voit, G. M. 2004, in *Clusters of Galaxies: Probes of Cosmological Structure and Galaxy Evolution*, ed. J. S. Mulchaey, A. Dressler, & A. Oemler, 143
- Eastman, J., Martini, P., Sivakoff, G., Kelson, D. D., Mulchaey, J. S., & Tran, K.-V. 2007, *ApJ*, 664, L9
- Edge, A. C., Stewart, G. C., Fabian, A. C., & Arnaud, K. A. 1990, *MNRAS*, 245, 559
- Eilek, J. A. & Owen, F. N. 2006, *ArXiv Astrophysics e-prints*, astro-ph/0612111
- Eisenstein, D. J. & Hu, W. 1999, *ApJ*, 511, 5
- Fabian, A. C. 2002, in *Lighthouses of the Universe: The Most Luminous Celestial Objects and Their Use for Cosmology: Proceedings of the MPA/ESO/MPE/USM Joint Astronomy Conference Held in Garching, Germany, 6-10 August 2001*, ESO ASTROPHYSICS SYMPOŠIA. ISBN 3-540-43769-X. Edited by M. Gilfanov, R. Sunyaev, and E. Churazov. Springer-Verlag, 2002, p. 24, ed. M. Gilfanov, R. Sunyaev, & E. Churazov, 24
- Fabian, A. C., Sanders, J. S., Allen, S. W., Crawford, C. S., Iwasawa, K., Johnstone, R. M., Schmidt, R. W., & Taylor, G. B. 2003, *MNRAS*, 344, L43
- Finoguenov, A., Reiprich, T. H., & Böhringer, H. 2001, *A&A*, 368, 749
- Fujita, Y., Matsumoto, T., & Wada, K. 2004, *Journal of Korean Astronomical Society*, 37, 571
- Fujita, Y., Suzuki, T. K., Kudoh, T., & Yokoyama, T. 2007, *ApJ*, 659, L1
- Gantner, B., Burns, J. O., & Hallman, E. J. 2007, in preparation
- Gao, L., White, S. D. M., Jenkins, A., Frenk, C. S., & Springel, V. 2005, *MNRAS*, 363, 379
- Gentile, G., Rodríguez, C., Taylor, G. B., Giovannini, G., Allen, S. W., Lane, W. M., & Kassim, N. E. 2007, *ApJ*, 659, 225
- Gómez, P. L., Loken, C., Roettiger, K., & Burns, J. O. 2002, *ApJ*, 569, 122
- Haiman, Z., Mohr, J. J., & Holder, G. P. 2001, *ApJ*, 553, 545
- Hallman, E. J. & Markevitch, M. 2004, *ApJ*, 610, L81
- Hallman, E. J., Motl, P. M., Burns, J. O., & Norman, M. L. 2006, *ApJ*, 648, 852
- Hallman, E. J., Wagner, R., Motl, P. M., Burns, J. O., & Norman, M. L. 2007, in preparation
- Heinz, S., Reynolds, C. S., & Begelman, M. C. 1998, *ApJ*, 501, 126
- Ikebe, Y., Makishima, K., Ezawa, H., Fukazawa, Y., Hirayama, M., Honda, H., Ishisaki, Y., Kikuchi, K., Kubo, H., Murakami, T., Ohashi, T., Takahashi, T., & Yamashita, K. 1997, *ApJ*, 481, 660
- Jeltema, T. E., Hallman, E. J., Burns, J. O., & Motl, P. M. 2007, *ArXiv e-prints*, 0708.1518J
- Kaiser, N. 1986, *MNRAS*, 222, 323
- Kravtsov, A. V., Nagai, D., & Vikhlinin, A. A. 2005, *ApJ*, 625, 588
- Lewis, A. D., Stocke, J. T., & Buote, D. A. 2002, *ApJ*, 573, L13
- Lin, Y.-T., Mohr, J. J., & Stanford, S. A. 2003, *ApJ*, 591, 749
- Loken, C., Melott, A. L., & Miller, C. J. 1999, *ApJ*, 520, L5
- Loken, C., Norman, M. L., Nelson, E., Burns, J., Bryan, G. L., & Motl, P. 2002, *ApJ*, 579, 571
- Makino, N. & Asano, K. 1999, *ApJ*, 512, 9
- Markevitch, M., Gonzalez, A. H., David, L., Vikhlinin, A., Murray, S., Forman, W., Jones, C., & Tucker, W. 2002, *ApJ*, 567, L27
- Markevitch, M. & Vikhlinin, A. 2007, *Phys. Rep.*, 443, 1
- Mathews, W. G., Faltenbacher, A., & Brighenti, F. 2006, *ApJ*, 638, 659
- Mazzotta, P., Rasia, E., Moscardini, L., & Tormen, G. 2004, *MNRAS*, 354, 10
- McCarthy, I. G., Babul, A., Bower, R. G., & Balogh, M. L. 2007a, *ArXiv e-prints*, 0706.2768
- McCarthy, I. G., Bower, R. G., & Balogh, M. L. 2007b, *MNRAS*, 377, 1457
- Mo, H. J. & White, S. D. M. 1996, *MNRAS*, 282, 347
- Motl, P. M., Burns, J. O., Loken, C., Norman, M. L., & Bryan, G. 2004, *ApJ*, 606, 635
- Motl, P. M., Hallman, E. J., Burns, J. O., & Norman, M. L. 2005, *ApJ*, 623, L63
- Mulchaey, J. S. 2004, in *Clusters of Galaxies: Probes of Cosmological Structure and Galaxy Evolution*, ed. J. S. Mulchaey, A. Dressler, & A. Oemler, 353
- Nagai, D., Vikhlinin, A., & Kravtsov, A. V. 2007, *ApJ*, 655, 98
- Navarro, J. F., Frenk, C. S., & White, S. D. M. 1997, *ApJ*, 490, 493
- O'Hara, T. B., Mohr, J. J., Bialek, J. J., & Evrard, A. E. 2006, *ApJ*, 639, 64
- O'Shea, B. W., Bryan, G., Bordner, J., Norman, M. L., Abel, T., Harkness, R., & Kritsuk, A. 2004, *Adaptive Mesh Refinement Ú Theory and Applications*, ed. T. Plewa, T. Linde, & G. Weirs (Springer-Verlag)
- Peres, C. B., Fabian, A. C., Edge, A. C., Allen, S. W., Johnstone, R. M., & White, D. A. 1998, *MNRAS*, 298, 416

- Peterson, J. R., Kahn, S. M., Paerels, F. B. S., Kaastra, J. S., Tamura, T., Bleeker, J. A. M., Ferrigno, C., & Jernigan, J. G. 2003, *ApJ*, 590, 207
- Ponman, T. J., Sanderson, A. J. R., & Finoguenov, A. 2003, *MNRAS*, 343, 331
- Poole, G. B., Fardal, M. A., Babul, A., McCarthy, I. G., Quinn, T., & Wadsley, J. 2006, *MNRAS*, 373, 881
- Rasia, E., Mazzotta, P., Borgani, S., Moscardini, L., Dolag, K., Tormen, G., Diaferio, A., & Murante, G. 2005, *ApJ*, 618, L1
- Rasia, E., Etti, S., Moscardini, L., Mazzotta, P., Borgani, S., Dolag, K., Tormen, G., Cheng, L. M., & Diaferio, A. 2006, *MNRAS*, 369, 2013
- Ricker, P. M. & Sarazin, C. L. 2001, *ApJ*, 561, 621
- Ritchie, B. W. & Thomas, P. A. 2002, *MNRAS*, 329, 675
- Ruszkowski, M. & Begelman, M. C. 2002, *ApJ*, 581, 223
- Ruszkowski, M., Brüggén, M., & Begelman, M. C. 2004, *ApJ*, 611, 158
- Sadat, R., Blanchard, A., Vauclair, S. C., Lumb, D. H., Bartlett, J., Romer, A. K., Bernard, J.-P., Boer, M., Marty, P., Nevalainen, J., Burke, D. J., Collins, C. A., & Nichol, R. C. 2005, *A&A*, 437, 31
- Spergel, D. N., Bean, R., Doré, O., Nolta, M. R., Bennett, C. L., Dunkley, J., Hinshaw, G., Jarosik, N., Komatsu, E., Page, L., Peiris, H. V., Verde, L., Halpern, M., Hill, R. S., Kogut, A., Limon, M., Meyer, S. S., Odegard, N., Tucker, G. S., Weiland, J. L., Wollack, E., & Wright, E. L. 2007, *ApJS*, 170, 377
- Valdarnini, R. 2006b, *New Astronomy*, 12, 71
- Vikhlinin, A., Burenin, R., Forman, W. R., Jones, C., Hornstrup, A., Murray, S. S., & Quintana, H. 2006a, *ArXiv Astrophysics e-prints*, astro-ph/0611438
- Vikhlinin, A., Kravtsov, A., Forman, W., Jones, C., Markevitch, M., Murray, S. S., & Van Speybroeck, L. 2006b, *ApJ*, 640, 691
- Voit, G. M. & Donahue, M. 2005, *ApJ*, 634, 955
- Wang, L. & Steinhardt, P. J. 1998, *ApJ*, 508, 483
- White, D. A., Jones, C., & Forman, W. 1997, *MNRAS*, 292, 419
- White, S. D. M. & Rees, M. J. 1978, *MNRAS*, 183, 341
- Wise, M. W., McNamara, B. R., Nulsen, P. E. J., Houck, J. C., & David, L. P. 2007, *ApJ*, 659, 1153
- Zabludoff, A. I. & Mulchaey, J. S. 1998, *ApJ*, 496, 39
- Zakamska, N. L. & Narayan, R. 2003, *ApJ*, 582, 162